Redox-dependent Franck-Condon blockade and avalanche transport in a graphene-fullerene single-molecule transistor

Chit Siong Lau,[†] Hatef Sadeghi,[‡] Gregory Rogers,[†] Sara Sangtarash,[‡] Panagiotis Dallas,[†] Kyriakos Porfyrakis,[†] Jamie Warner,[†] Colin J. Lambert,[‡] G. Andrew D. Briggs,[†] and Jan A. Mol[*,†]

Department of Materials, University of Oxford, 16 Parks Road, Oxford OX1 3PH, UK, and Quantum Technology Center, Physics Department, Lancaster University, Lancaster LA1 4YB, UK

E-mail: jan.mol@materials.ox.ac.uk

Abstract

We report transport measurements on a graphene-fullerene single-molecule transistor. The robust architecture where a functionalised C_{60} binds to graphene nanoelectrodes results in strong electron-vibron coupling and weak vibron relaxation. Using a combined approach of transport spectroscopy, Raman spectroscopy and DFT calculations, we demonstrate center-of-mass oscillations, redox-dependent Franck-Condon blockade and a transport regime characterized by avalanche tunnelling in a single-molecule transistor.

Coupling between electronic and vibrational degrees of freedom in single-molecule devices can lead to transport properties very different from those of metal/semiconductor nanostructures.[1] Charge transfer can excite vibrational modes,[2] or vibrons, and strong electron-vibron coupling leads to suppression of tunnel current at low bias.[3,4] Theory further predicts super-Poissonian current noise, characterised by giant Fano factors, for molecular junctions with weak vibron-relaxation owing to avalanche-type charge transfer.[5] Here, we demonstrate a robust architecture of a single-molecule transistor where a functionalised C_{60} binds to graphene nano-electrodes via $\pi - \pi$ interactions. The stability and weak vibron-relaxation of our system enables us to investigate redox-dependent electron-vibron coupling and avalanche transport.

We perform transport measurements of graphene-fullerene single-molecule transistors fabricated using feedback-controlled electroburning.[6] The molecule bridging the graphene nano-gap is a pyrene functionalised C_{60} bisadduct synthesised through a 1,3 dipolar cycloaddition using 1-pyrene carboxaldehyde and N-methylglycine (Supplementary section 1.1).[7] While the functionalisation results in different isomers, steric considerations mean only the cis-2 and cis-3 isomers are expected to bridge the graphene nano-gap. Density Functional Theory (DFT) calculations of the relaxed graphene-fullerene-graphene structure confirm that the cis-3 isomer forms the most stable configuration without steric hindrance, as shown in Figure 1a. Iso-surfaces of the frontier orbitals of gas phase cis-3 isomer are shown in Figure

[*]To whom correspondence should be addressed

[†]Department of Materials, University of Oxford, 16 Parks Road, Oxford OX1 3PH, UK

[‡]Quantum Technology Center, Physics Department, Lancaster University, Lancaster LA1 4YB, UK

1b.[8] The wavefunction of the lowest unoccupied molecular orbital (LUMO) level is mostly localized in the central C_{60}, whereas for the highest occupied molecular orbital (HOMO) level, the wavefunction is extended to the pyrene anchors. Comparison of the iso-surfaces of frontier orbitals for cis-2 and cis-3 isomers further show that the wavefunction delocalization of the HOMO levels are more pronounced in the cis-3 isomer, indicating that it has a better π-π interaction with the graphene electrodes and is therefore more likely to bridge the junction (Supplementary Figure S11). In pristine C_{60}, DFT predicts LUMO dominated transport which was verified with thermoelectric experiments.[9] In contrast, our DFT calculations predict that charge transport in the bisadduct is more likely to be HOMO dominated.[10,11]

Figure 1c shows the current I as a function of bias V_b and gate V_g voltage of a single-molecule transistor (device A), measured at 20 mK. The addition energies between adjacent redox states, measured from the height of the Coulomb diamonds, are $E_{\mathrm{add}} \sim 160$ meV for all charge-state transitions. We attribute the absence of odd/even oscillations of E_{add}, previously observed for two-fold spin shell systems,[6,12] to orbital degeneracies of the C_{60} molecule.[13] Calculations have shown that the interactions within each shell in C_{60} are almost constant, with only a slight increase of the electron-electron on-site Coulomb interaction in the middle of each shell where electrons with opposite spins begin to fill.[13] We observe a small increase of ~ 10 meV per electron added from charge state N to $N+2$ which we attribute to the on-site Coulomb interactions. In the constant interaction model E_{add} is given by the sum of the charging energy E_C, due to Coulomb interactions of the electrons in the molecule, and the energy gap Δ_{HL} between the HOMO and LUMO.[14] For a two-fold degenerate system, E_{add} oscillates between E_C and $E_C + \Delta_{\mathrm{HL}}$, while for systems with higher degeneracies, $E_{\mathrm{add}} = E_C$ until a level is completely filled. From the fact that E_{add} here is constant for three charge-state transitions, we infer that electrons are filling exclusively a HOMO that is at least four-fold degenerate. This is consistent

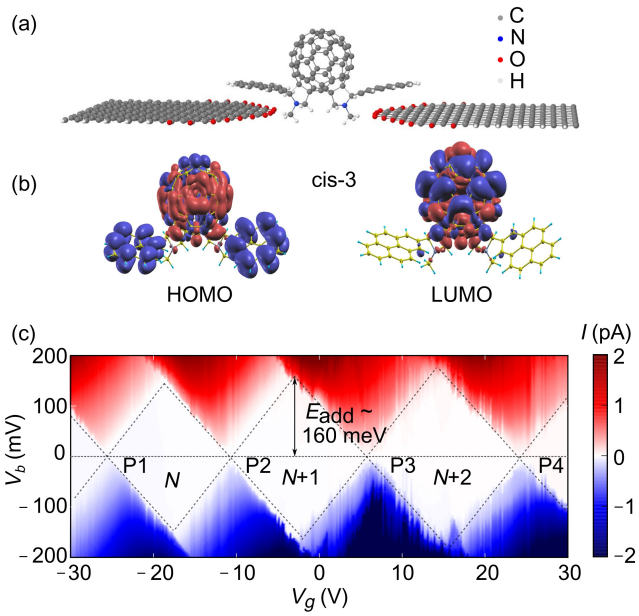

Figure 1: (a) DFT calculations showing the relaxed structure of the cis-3 isomer bridging the graphene nano-gap. The electrodes are fabricated using feedback-controlled electroburning of chemical vapour deposition grown graphene transferred to a heavily doped silicon substrate with a 300 nm thick silicon oxide layer, which also serves as a back-gate that electrostatically modulates the chemical potential of the molecule. The molecules are deposited on the electrodes from a chloroform solution (Methods). (b) DFT simulations of the iso-surfaces of the LUMO and HOMO of cis-3 isomer. (c) Current stability diagram of device A. All measurements are performed at 20 mK unless otherwise stated. Within each diamond, the system is in Coulomb blockade (CB) and the charge on the molecule is stable. The molecular redox state changes by one between adjacent diamonds.

with our DFT prediction of HOMO dominated transport and calculations of the Kohn-Sham HOMO and LUMO energies, which show that the HOMO (-4.59 eV) and HOMO-1 (-4.60 eV) levels are almost degenerate in energy, in contrast to the LUMO (-3.12 eV) and LUMO+1 (-2.86 eV) levels (Supplementary section 2.3).

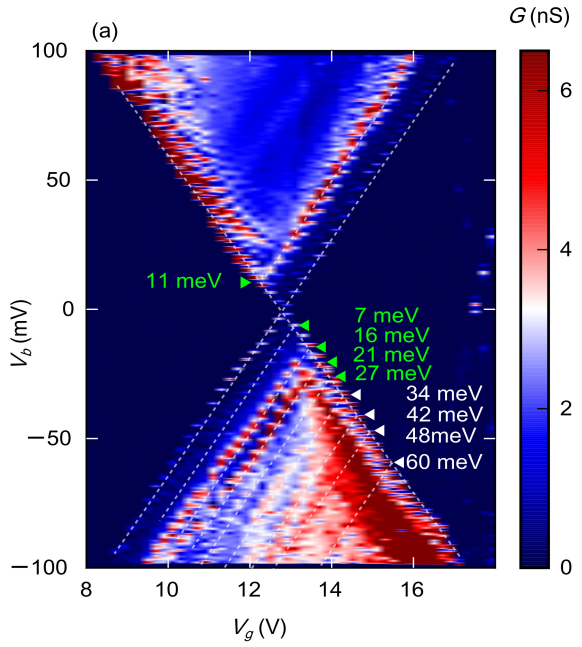

Figure 2: (a) Conductance stability diagram of the $N+1$ to $N+2$ transition (P3 in Figure 1c) obtained by taking the numerical derivative of the current measured. Excited states are indicated by the white and green arrows. Details on how the excited states are determined are included in Supplementary section 1.5.

Figure 2 shows a map of the differential conductance G of charge transition $N+1$ to $N+2$ of device A taken with a higher resolution (P3 in Figure 1c). The gate potential for the charge transition is different for repeated measurements due to a common hysteretic effect likely related to charge traps in the oxide. The effect occurs when the gate potential is swept quickly across a large range, but is otherwise stable when swept slowly. We observe lines corresponding to excited state transitions at energies ≥ 33 meV (white arrows) that are in excellent agreement with the intrinsic vibrational modes of pristine C_{60},[15] as summarized in Table 1. We also observe excited states at energies < 33 meV (green arrows), below the lowest vibrational mode of the pristine C_{60}. The asymmetry of the excited states on the bias polarity can be explained through a rate equation model involving asymmetric tunnelling barriers, which was previously observed in the orbital excited state spectrum of a single donor in silicon. When the excited state relaxations are fast compared to the tunneling rates, an electron can tunnel on to the molecule through any number of excited states that lie within the bias window but only leave through the ground state as the molecule relaxes. In the limit where the molecule-electrodes coupling is very asymmetric, current steps are not expected for one bias polarity.[16]

A comparison of the transport spectroscopy and Raman spectra of pristine C_{60} and bisadduct (Table 1) indicates that these excited state transitions have a vibrational nature. To identify the mechanical motion of these additional low-lying vibrational modes, we use DFT results where we analyse the mechanical degrees of freedom of the bisadduct in the limit where the atomic mass of the pyrene anchor groups approach infinity (Supplementary section 2.6). In this limit, the anchor groups are effectively clamped and the modes corresponding to internal vibrations of the pyrene are filtered from the vibrational spectrum. DFT calculations in this limit reveal six vibrational modes at energies < 33 meV, with two sets of three modes each corresponding to the translational and rotational center-of-mass motion of the central C_{60} with respect to the anchor groups (Supplementary Figure S13a, animations in Supplementary Information).

Mode	Energy (meV)			
	Transport (this work)	Raman (this work)	DFT (this work)	C_{60} (Ref.[15])
CM T_y	7		8	
CM T_x			10	
CM R_z	11	13	12	
CM T_z	16	16	16	
CM R_x	21	19	19	
CM R_y	27	25	21	
$H_g(1)$	34	33	32, 33, 34	33
$T_{2u}(1)$	42			43
$G_u(1)$	42			43
$H_g(2)$	48	55		53
$A_g(1)$	60	61		61

Table 1: Comparison between measured excitation energies from transport and Raman spectroscopy, calculated values and intrinsic vibrational modes of pristine C_{60}. Transport measurements are performed at 20 mK in vacuum with the molecule anchored to graphene electrodes. Raman spectroscopy is performed at room temperature with the molecules drop-casted on to gold coated silicon substrates to enhance the Raman scattering. DFT calculations are performed with the condition where the degrees of motion of the anchor groups are completely restricted in order to elucidate the center-of-mass motions. In the actual system, the pyrene groups are expected to exhibit small motions. The values for the vibrational modes of pristine C_{60} are obtained from.[15] We find that the discrepancies between our measurements fall within the range of values reported in ref. 18, which are obtained from experiments and *ab initio* theories reported by different groups and can differ by up to 10 meV.

Figure 3 shows low energy excitations observed for all four charge transitions (P1-4 in Figure 1c) with spacings of 1.7 meV (P1), 1.5 meV (P2) 1.7 meV (P3) and 1.5 meV (P4) (white arrows). Low energy excitations are similarly observed in measurements of device B (∼2 meV, Supplementary Figure S7a). Lines with different slopes, corresponding to different capacitive couplings, are probably not related to the energy spectrum of the molecule. They can be from a different Coulomb diamond related to a separate quantum dot located close to the device or associated with density of states fluctuations in the graphene electrodes. Similar fluctuations have also been observed in silicon SETs.[17] To account for the nature of the low energy excitations (∼ 2 meV), we analyse the vibrational modes of the bisadduct using DFT where all the mechanical degrees of freedom of the atoms are allowed (Supplementary section 2.6). The lowest non-zero mode is at 1.7 meV, consistent with our measurements (Supplementary Figure S13b). This mode is due to the combined center-of-mass motions of the central C_{60} and pyrene anchors moving perpendicularly relative to each other, with the central

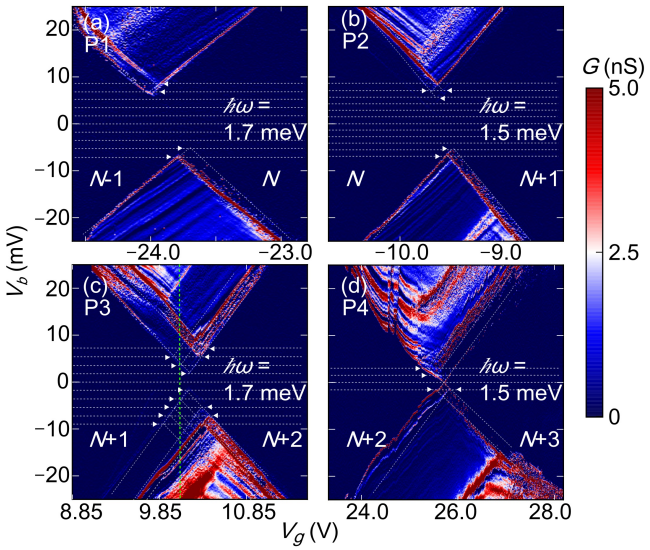

Figure 3: (a-d) Conductance stability diagrams for transitions $N-1$ to $N+3$. The low bias current suppression is due to FC blockade in systems with strong electron-vibron coupling. Sets of integer spaced vibrational state lines (white arrows) are observed in the low bias regime. The vertical green line in (c) is the gate voltage at which the large current noise discussed in Figure 5 is measured. The energy of a single vibrational quantum, $\hbar\omega$, is extracted for all 4 charge transitions (Supplementary section 1.5). These energy spacings are determined by first fitting the peaks of the excited state transitions at two different V_g to a thermally broadened Lorentzian in order to extract the peak position and slopes. $\hbar\omega$ is then determined by the intersection of the excited state lines with the Coulomb diamond edges.

C_{60} moving out-of-plane while the anchors move in-plane (animation in Supplementary Information). Our findings are consistent with a previous report that the binding energy of pyrene to graphene is much stronger out-of-plane compared to in-plane, such that the pyrene anchors can more easily slide on the graphene electrodes.[18]

The Coulomb diamond edges do not intersect at zero bias for P1 to 3 (Figure 3a-c) and in device C (Supplementary Figure S7b). The current suppression at low bias remain unchanged with the application of a magnetic field, ruling out a magnetic origin (Supplementary Figure S6)[19] and the size of the gaps correspond to an integer spacing of the energy excitations. We attribute these features to Franck-Condon (FC) blockade that occurs for strong electron-vibron coupling,[5] illustrated in Figure 5a. Electrons tunnelling onto the molecule shifts the equilibrium coordinates of the harmonic oscillator wavefunctions for charge states N and $N+1$ by an amount proportional to the dimensionless electron-vibron coupling constant λ. For strong coupling, $\lambda \gg 1$, the equilibrium coordinates of the $N+1$ charge state is greatly displaced from that of the N charge state (Figure 5a). As a result, the transition rate between the vibronic ground states of charge states N and $N+1$, determined by the overlap of the vibron wavefunctions, is exponentially reduced with λ, leading to current suppression at low bias. The FC blockade is lifted when the applied bias is sufficiently large for transitions from the vibronic ground state to higher excited states (Figure 5c), where the transition rates are higher from increased overlap of the vibronic wavefunctions. When electrons are added to the molecule, we observe a decrease of the FC gap from P2 to P4, such that for P4 (Figure 3d), the FC blockade is completely lifted. The FC gap, i.e. the threshold voltage at which the FC blockade is lifted when it matches a multiple of the vibrational quantum $n\hbar\omega$, is proportional to $\lambda^2\hbar\omega$.[5] Additional electrons on the molecule shift the equilibrium positions of the harmonic oscillator wavefunctions, leading to a smaller displacement of the equilibrium coordinates between charge states $N+2$ and $N+3$, i.e. a smaller λ. The higher transition rate for the vibronic ground states from the increased wavefunction overlap allows for current in the previously FC blockade region. Redox dependent electron-vibron coupling is possibly due to Jahn-Teller (JT) distortion of the molecule,[20] which is particularly strong in molecules with a large orbital degeneracy and high spatial symmetry such as C_{60}.[21] The geometrical JT distortion lowers the overall ground state energy which is directly proportional to λ, as derived in ref. 23. Our observation of HOMO degeneracy and a charge state dependent λ is therefore in line with these predictions.

Using the set of evenly spaced excitations of P3 (Figure 3c) and fitting them to the rate equation model,[22] we determine $\lambda = 3.0$ for the charge transition $N+1$ to $N+2$ (Supplementary section 1.5). We simulate the stability diagram for an asymmetric molecule-electrode tunnel coupling, dependent on the contact geometry of the molecule to the electrodes, $t_L = 0.2t_R$ (Figure 4b), which shows good qualitative agreement with our measurements (Figure 4a). The electroburnt graphene nano-electrodes are not likely to be symmetric on the atomic scale which can lead to asymmetric positioning of the molecule across the junction. Furthermore, our DFT calculations show that the pyrene anchors are not symmetric relative to the central C_{60} (Supplementary section 2.2).

At elevated temperatures T, the thermal equilibrium population of vibrational excited states, with exponentially greater transition rates, are increased,[3,4] and transitions at low bias can now proceed via these states. In device A the FC gap is lifted at 3 K (Figure 4c,d), and device C at 4 K (Supplementary Figure S7b,c). We extract and fit the temperature dependence of $I \propto 1/k_BT \times 1/(exp(\hbar\omega/k_BT)-1)$[3,4] at $V_g = 7$ V and $V_b = 7.2$ mV in Figure 4c and obtained a value of $\hbar\omega = 1.7$ meV (Supplementary Figure S8), accordant with the value measured in Figure 3c. The increase of peak intensity with temperature is in direct contrast with the case for which a Fermi-Dirac distribution is relevant, where a decrease is expected, $I \propto 1/k_BT$.[3] These observation confirms the bosonic nature of the transition and is consistent with our in-

terpretation of the FC model.

Low energy excitations (3 to 7 meV) were previously observed for a pristine C_{60} single-molecule transistor connected to gold electrodes.[2] Those excitations were attributed to nanomechanical oscillations arising from the center-of-mass motion of the C_{60} and no FC blockade was observed. This is due to the different coupling mechanisms for internal molecular vibrations and center-of-mass oscillations. While vibrations couple directly to the electron, oscillations instead couple through displacement dependent tunneling matrix elements.[22] At energies below 10 meV, it has been shown that the coupling strength for oscillations is insufficient to induce FC blockade.[4] The observation of FC blockade from the 1.7 meV excitation in our device is consistent with this interpretation and our DFT calculations which showed that the 1.7 meV mode is related to a combined vibration of the central C_{60} and the pyrene anchor groups.

Strong electron-vibron coupling and weak vibron relaxation can further lead to avalanche transport characterised by strong current fluctuations.[5] These fluctuations are the result of occasional charge transfer events exciting the molecule from its vibrational ground state and setting off an avalanche of electrons tunneling via vibrational excited states that have greater wavefunction overlap, as shown in Figure 5a-f. An avalanche is terminated when the molecule returns to its ground state by tunneling induced de-excitation or dissipative relaxation. Figure 5g shows that avalanche transport, in contrast to field-induced bi-stabilities,[23] leads to fluctuations that persist over the entire bias range corresponding to the vibrational $0 \leftrightarrow 2$ transition. For $\beta eV_b < 2\hbar\omega$ ($\beta \sim 0.5$ given by the ratio of the source capacitance and the total capacitance), the vibrational transitions $0 \leftrightarrow 0$ and $0 \leftrightarrow 1$ are suppressed due to FC blockade (a,d). At $2\hbar\omega \leq \beta eV_b < 3\hbar\omega$, the $0 \leftrightarrow 2$ transition enters the bias window (Figure 5b,e). While the transition rate is higher, the system typically experiences a long wait time with no current while it remains in the vibron ground state. For weak vibron relaxation, occasional electron inelastic tunnelling excites the

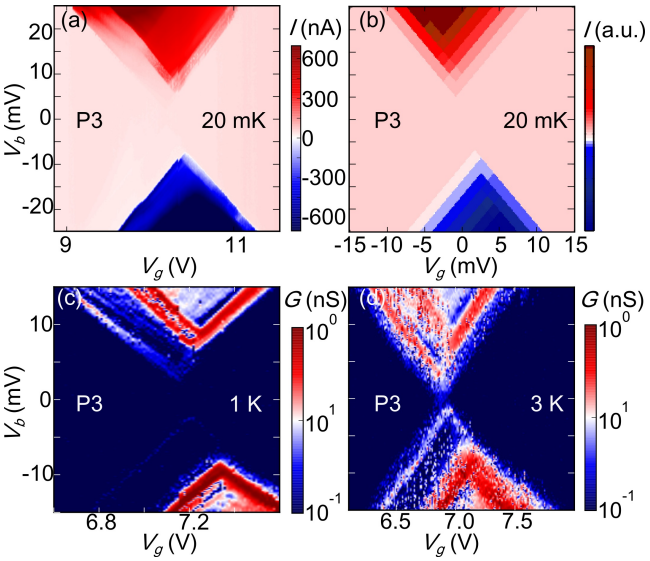

Figure 4: (a) Current stability diagram of P3 at 20 mK. (b) Simulated current stability diagram using the rate equation model with $\lambda = 3$ and $t_L = 0.2t_R$, showing good qualitative agreement with (a). Conductance stability diagrams of P3 at 1 K (c) and 3 K (d). The FC gap is lifted at 3 K. Transitions due to vibron absorption are described by Bose-Einstein statistics, such that $I_{\text{step}} \propto 1/k_BT \times 1/(exp(\hbar\omega/k_BT) - 1)$. We extract and fit the temperature dependence of I at $V_g = 7$ V and $V_b = 7.2$ mV in Figure 3c and obtained a value of $\hbar\omega = 1.7$ meV, consistent with our experimentally determined value.

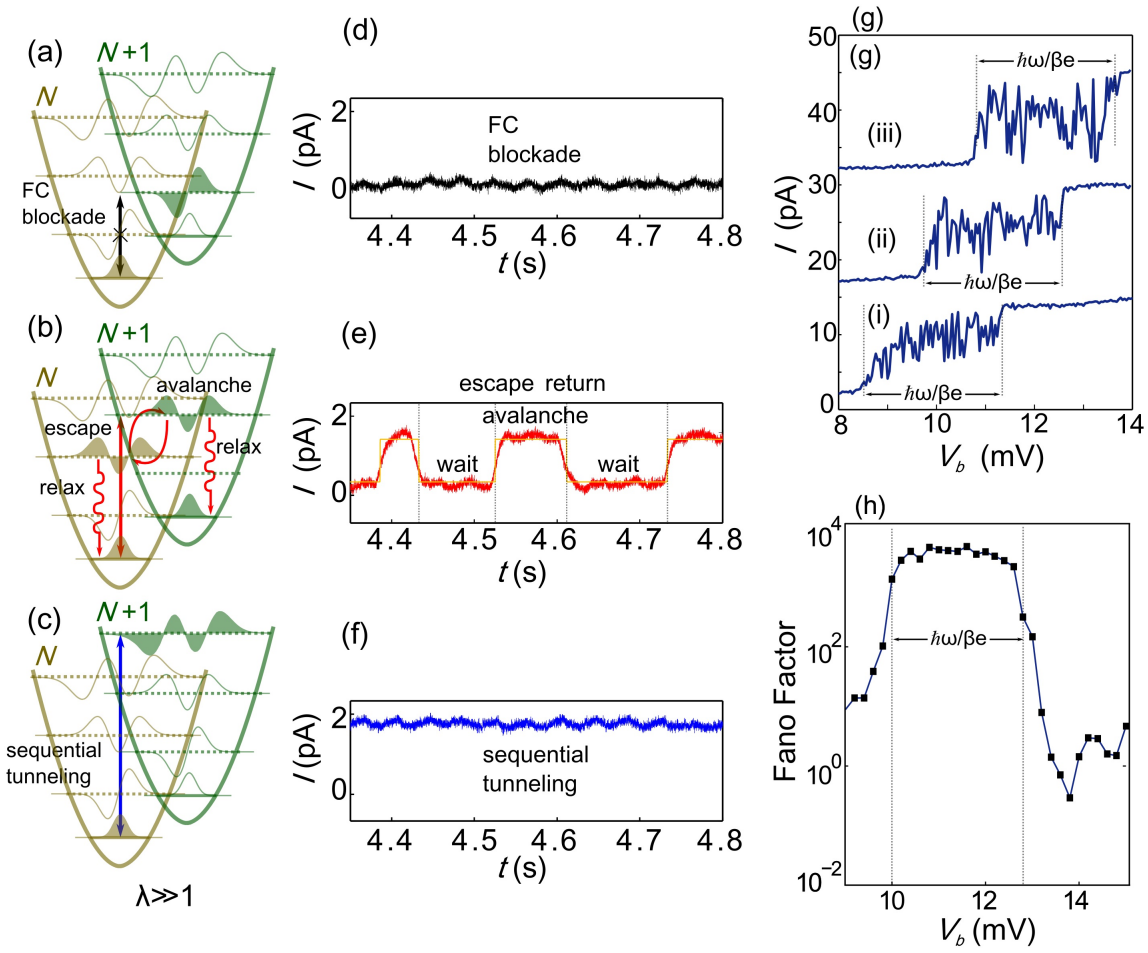

Figure 5: (a-c) Schematics for avalanche transport. (d-f) Current-time traces at $V_b = 9$, 12 and 14 mV. The full current-time trace over which we perform the HMM fit was measured for 20 s with a 100 kHz sampling rate. The orange curve (e) is the HMM fit to the full current-time trace. (g) IV at $V_g =$ (i) 10.1 V, (ii) 10.15 V and (iii) 10.2 V. Curves are offset for clarity, +15 pA (ii) and +30 pA (iii). The current noise extends over an applied bias corresponding to $\hbar\omega/\beta e$. (h) Fano factors of the zero-frequency noise measured as a function of V_b at $V_g = 10.15$ V indicated by the green line in Figure 3c. Giant Fano factors $\sim 10^3$ extend over an applied bias corresponding to $\hbar\omega/\beta e$, reflecting avalanche transport, before decreasing to ~ 1 at higher bias in accordance with sequential tunnelling.

molecule to a higher vibrational state, with subsequent tunnelling events further increasing this excitation. Having escaped the ground state, an avalanche of tunnelling events occur. The process terminates when the system returns to the vibrational ground state, resulting in another long wait time before the cycle repeats. At $\beta eV_b \geq 3\hbar\omega$, charge transfer proceeds via sequential tunnelling through the $0 \leftrightarrow 3$ transition (Figure 5c,f).

To characterise the current fluctuations we extract the $0 \leftrightarrow 2$ escape and return rates by fitting a current–time trace of device A measured at $V_b = 12$ mV to a Hidden Markov Model (HMM) assuming a two state stochastic process (orange line in Figure 5e).[24] We obtain an escape rate of 15 ± 2 s^{-1}, which corresponds to a FC matrix element $W_{0\leftrightarrow 2} \sim 0.002$ and $\lambda \sim 4$ (Supplementary section 1.9), and a return rate of 22 ± 2 s^{-1}. These rates place an upper-bound of ~ 1 s^{-1} on the dissipative relaxation rate. The observation of such a slow relaxation rate, compared to values measured in time resolved spectroscopy (~ 1 ps^{-1}),[25] is indeed surprising. However, those measurements are usually performed in a solvent where dissipation to solvent ions is possible. Low temperature and vacuum conditions suppresses the dissipation rate,[26] which is mostly dependent on dissipation to the electrodes in single-molecule junctions.[10,27] Fits of the conductance peaks (Supplementary section 1.5) show that the pyrene anchors form weak π-π stacking interactions with the graphene electrode (molecule-electrode coupling t_0 $\sim$1 meV). While the in-plane thermal conductivity of graphene is exceptionally large, its out-of-plane thermal conductivity is limited by weak van der Waals interactions between adjacent planes and substrates and can possibly suppress vibron dissipation to the graphene electrodes.[28] Vibrationally induced conformational changes where an anharmonic potential with local minimas suppress dissipation is another possibility.[1] Metastable molecular conformation can be long lived on the order of milliseconds, consistent with the return rates in our system, and can be accessed through a vibrational excited state.[29] Dissipation to the electrodes is dependent on the atomistic details of the vibron density of states at the molecule-electrode interface. The non-equilibrium distribution of vibrons is non-trivial and requires a self-consistent calculation of electron-vibron dynamics.

Electron avalanche transport is characterized by giant Fano factors on the order of 10^2-10^3 occurring in steps over the bias window ($\hbar\omega/\beta e$) corresponding to a vibron transition.[5] The zero frequency Fano factor $F = S/2e\langle I\rangle$ for the excess noise $S(0) - S(0)_{V_b=0}$ indicates the deviation from Poissonian noise, where $F = 1$. The noise power density $S(\omega)$ is defined as the Fourier transform of the current-current correlation,

$$S(\omega) = \int_{-\infty}^{\infty} dt e^{i\omega t} \langle \delta I(t+t')\delta I(t')\rangle_{t'}. \quad (1)$$

In Figure 5h, we determine the zero frequency Fano factors as a function of V_b (Supplementary section 1.9), taken at $V_g = 10.15$ V indicated by the vertical green line in Figure 3c. At $10 \leq V_b \leq 13$ mV, the Fano factors increase to an order of $\sim 10^2 - 10^3$, reflecting the current fluctuations due to avalanche transport. These giant Fano factors likewise persist over an applied bias corresponding to $\hbar\omega$. When V_b is sufficient to lift FC blockade, the Fano factor is expected to return to values of the order of 1.[5] At $V_b = 13.4$ mV, the Fano factors decrease to ~ 1 in accordance with sequential transport.[30]

We have demonstrated a robust architecture using functionalised C_{60} bisadduct and graphene electrodes to create single-molecule transistors which enables the observation of redox-dependent FC blockade and avalanche transport. While doping-induced variations in the Fermi-level of the graphene electrodes and offset charges in the oxide can influence the alignment of the electrochemical potential of the molecule with the Fermi-level of the graphene electrodes, we show that the functionalisation of C_{60} with pyrene anchors groups can modify electron delocalization and energy levels leading to HOMO dominated transport, in contrast to previous reports of LUMO domi-

nated transport in C_{60} transistors.[10] Calculations have suggested that the modification of electron delocalization and energies via the inclusion of side group can be used to tune the thermopower of single-molecule junctions.[31,32] Furthermore, thermoelectric efficiency is maximised when charge transport across a junction occurs through a single level with low vibrational heat conductance.[32] Therefore, the observation of an extremely long vibron lifetime not only offers unique potential for the fundamental study of quantized motion and thermal transport on the nanoscale, but is also promising for practical applications in single-molecule energy-conversion devices.[32]

Methods

Device Fabrication and Measurements

The molecular devices are fabricated on a heavily doped silicon chip with a 300 nm thick oxide which also serves as a back gate to modulate charge transport through the junction. First, graphene is synthesized on liquid copper supported on a tungsten substrate using chemical vapour deposition.[33] Using a wet transfer technique, the graphene is transferred to the silicon substrate with pre-patterened gold electrodes. The graphene electrodes are fabricated based on the method of feedback-controlled electroburning.[34] Fabricated nanogaps are typically between 1 to 2 nm. The devices are next immersed in a 10 μM chloroform solution containing the C_{60} bisadducts for 30 mins. We wirebond the devices to our sample puck and transfer them to our dilution fridge with a base temperature of 20 mK. All electrical measurements are performed using low noise, battery operated electronics, while the gate voltage was modulated with a Keithley 2400 sourcemeter.

DFT theoretical methods

To calculate the vibrational modes of the bisadducts, we use the Harmonic approximation method to construct the Dynamical Matrix D. The xyz coordinate of the two isomers of the bisadducts were constructed and the geometry relaxation were performed with Siesta[35] implementation of the Density Functional Theory (DFT) by double–ζ polarized bases set (DZP) and the GGA functional with PBE parameterization to the force tolerance of 20 meV/Å. A real-space grid is defined with an equivalent energy cut-off of 250 Ry. From the relaxed xyz coordinates of the system, a set of the xyz coordinates were generated by displacing each atom in positive and negative x, y and z directions by $\delta q' = 0.01$ Å. The forces in three directions $q_i = (x_i, y_i, z_i)$ on each atom were then calculated by DFT with the same parameters as the relaxed system but without geometry relaxation. These set of the force $F_i^q = (F_i^x, F_i^y, F_i^z)$ vectors are used to construct the Dynamical matrix (Supplementary section 2.1). The electronic structure and transport calculations are performed using GOLLUM as described in.[8]

References

(1) Galperin, M.; Ratner, M. A.; Nitzan, A. Journal of Physics: Condensed Matter **2007**, 19, 103201.

(2) Park, H.; Park, J.; Lim, A.; Anderson, E.; Alivisatos, A.; McEuen, P. Nature **2000**, 407, 57–60.

(3) Leturcq, R.; Stampfer, C.; Inderbitzin, K.; Durrer, L.; Hierold, C.; Mariani, E.; Schultz, M. G.; von Oppen, F.; Ensslin, K. Nature Physics **2009**, 5, 327–331.

(4) Burzurí, E.; Yamamoto, Y.; Warnock, M.; Zhong, X.; Park, K.; Cornia, A.; Van Der Zant, H. S. J. Nano Letters **2014**, 14, 3191–3196.

(5) Koch, J.; Von Oppen, F. Physical Review Letters **2005**, 94.

(6) Mol, J. A.; Lau, C. S.; Lewis, W. J. M.; Sadeghi, H.; Roche, C.; Cnossen, A.; Warner, J. H.; Lambert, C. J.; Anderson, H. L.; Briggs, G. A. D. Nanoscale **2015**, 7, 13181–13185.

(7) Maggini, M.; Scorrano, G.; Prato, M. Journal of the American Chemical Society **1993**, 115, 9798–9799.

(8) Sadeghi, H.; Mol, J. A.; Lau, C. S.; Briggs, G. A. D.; Warner, J.; Lambert, C. J. Proceedings of the National Academy of Sciences **2015**, 112, 2658–2663.

(9) Yee, S. K.; Malen, J. A.; Majumdar, A.; Segalman, R. A. Nano Letters **2011**, 11, 4089–4094.

(10) Schulze, G.; Franke, K. J.; Gagliardi, A.; Romano, G.; Lin, C. S.; Rosa, A. L.; Niehaus, T. A.; Frauenheim, T.; Di Carlo, A.; Pecchia, A.; Pascual, J. I. Physical Review Letters **2008**, 100, 136801.

(11) Al-Galiby, Q.; Grace, I.; Sadeghi, H.; Lambert, C. J. Journal of Materials Chemistry C **2015**, 3, 2101–2106.

(12) Kubatkin, S.; Danilov, A.; Hjort, M.; Cornil, J.; Brédas, J.-L.; Stuhr-Hansen, N.; Hedegård, P.; Bjørnholm, T. Nature **2003**, 425, 698–701.

(13) Ke, S.-H.; Baranger, H.; Yang, W. Physical Review Letters **2003**, 91, 116803.

(14) Kaasbjerg, K.; Flensberg, K. Nano letters **2008**, 8, 3809–14.

(15) Heid, R.; Pintschovius, L.; Godard, J. M. Physical Review B **1997**, 56, 5925–5936.

(16) Lansbergen, G. P.; Rahman, R.; Verduijn, J.; Tettamanzi, G. C.; Collaert, N.; Biesemans, S.; Klimeck, G.; Hollenberg, L. C. L.; Rogge, S. Phys. Rev. Lett. **2011**, 107, 136602.

(17) Fuechsle, M.; Miwa, J. a.; Mahapatra, S.; Ryu, H.; Lee, S.; Warschkow, O.; Hollenberg, L. C. L.; Klimeck, G.; Simmons, M. Y. Nature Nanotechnology **2012**, 7, 242–246.

(18) Bailey, S.; Visontai, D.; Lambert, C. J.; Bryce, M. R.; Frampton, H.; Chappell, D. The Journal of chemical physics **2014**, 140, 054708.

(19) Winkelmann, C. B.; Roch, N.; Wernsdorfer, W.; Bouchiat, V.; Balestro, F. Nat Phys **2009**, 5, 876–879.

(20) Lannoo, M.; Baraff, G. A.; Schlüter, M.; Tomanek, D. Physical Review B **1991**, 44, 12106–12108.

(21) O'Brien, M. C. M. **1993**, 61, 688.

(22) Koch, J.; Von Oppen, F.; Oreg, Y.; Sela, E. Physical Review B **2004**, 70, 1–12.

(23) Secker, D.; Wagner, S.; Ballmann, S.; Härtle, R.; Thoss, M.; Weber, H. B. Physical Review Letters **2011**, 106, 3–6.

(24) Greenfeld, M.; Pavlichin, D. S.; Mabuchi, H.; Herschlag, D. PLoS ONE **2012**, 7.

(25) Laubereau, A.; von der Linde, D.; Kaiser, W. Physical Review Letters **1972**, 28, 1162–1165.

(26) Kuznetsov, A. M.; Ulstrup, J. Journal of Electroanalytical Chemistry **2004**, 564, 209–222.

(27) Pascual, K. J. F.; Ignacio, J. Journal of Physics: Condensed Matter **2012**, 24, 394002.

(28) Pop, E.; Varshney, V.; a.K. Roy, A. K. MRS Bulletin **2012**, 37, 1273–1281.

(29) Eggeling, C.; Fries, J. R.; Brand, L.; GÃijnther, R.; Seidel, C. A. M. Proceedings of the National Academy of Sciences **1998**, 95, 1556–1561.

(30) Onac, E.; Balestro, F.; Trauzettel, B.; Lodewijk, C.; Kouwenhoven, L. Physical Review Letters **2006**, 96, 026803.

(31) Kim, Y.; Jeong, W.; Kim, K.; Lee, W.; Reddy, P. Nat Nano **2014**, 9, 881–885.

(32) Reddy, P.; Jang, S.-Y.; Segalman, R. A.; Majumdar, A. Science **2007**, 315, 1568–1571.

(33) Wu, Y. a.; Fan, Y.; Speller, S.; Creeth, G. L.; Sadowski, J. T.; He, K.; Robertson, A. W.; Allen, C. S.; Warner, J. H. ACS nano **2012**, 6, 5010–7.

(34) Lau, C. S.; Mol, J. A.; Warner, J. H.; Briggs, G. A. D. Physical chemistry chemical physics: PCCP **2014**, 16, 20398–401.

(35) Sánchez-Portal, J. M. S.; Artacho, E.; Gale, J. D.; García, A.; Junquera, J.; Ordejón, P.; Daniel, Journal of Physics: Condensed Matter **2002**, 14, 2745.

Acknowledgements

We thank the Royal Society for a Newton International Fellowship for J. A. M. and a University Research Fellowship for J. H. W., and the Agency for Science Technology and Research (A*STAR) for a studentship for C. S. L. This work is supported by Oxford Martin School, EPSRC grants EP/J015067/1, EP/K001507/1, EP/J014753/1, EP/H035818/1, EP/K030108/1 and the European Union Marie-Curie Network MOLESCO. This project/publication was made possible through the support of a grant from Templeton World Charity Foundation. The opinions expressed in this publication are those of the author(s) and do not necessarily reflect the views of Templeton World Charity Foundation.

Competing financial interests

The authors declare no competing financial interests.